catalysts

MDPI

Article

Coral Reef-like CdS/g-C_3N_5 Heterojunction with Enhanced CO_2 Adsorption for Efficient Photocatalytic CO_2 Reduction

Fuhai Zhang [1], Jing Xiong [2], Xiaoxiao Yu [1,2,3,*], Lei Wang [1], Tongyu Wu [1], Zhendong Yu [1], Minmeng Tang [1], Haiyan Liu [1], Yanhong Chao [2,*] and Wenshuai Zhu [1,*]

[1] State Key Laboratory of Heavy Oil Processing, College of Chemical Engineering and Environment, China University of Petroleum-Beijing, Beijing 102249, China; 2022210557@student.cup.edu.cn (F.Z.); 2023310260@student.cup.edu.cn (L.W.); 18617737801@163.com (T.W.); zjyzd123@cup.edu.cn (Z.Y.); mmtang@cup.edu.cn (M.T.); klc@cup.edu.cn (H.L.)
[2] Department of Applied Chemistry, College of Science, China University of Petroleum-Beijing, Beijing 102249, China; xiongjing@cup.edu.cn
[3] School of Chemistry and Chemical Engineering, Henan Normal University, Xinxiang 453007, China
* Correspondence: xiaoxiaoyu@cup.edu.cn (X.Y.); chaoyh@cup.edu.cn (Y.C.); zhuws@cup.edu.cn (W.Z.)

Abstract: As a promising member of the carbon nitride family, nitrogen-rich g-C_3N_5 has attracted significant attention because of its excellent light absorption performance. Nevertheless, its practical application in photocatalytic CO_2 reduction is hindered by severe photogenerated charge recombination and limited CO_2 adsorption capacity. Constructing a heterojunction has emerged as an effective strategy to mitigate charge recombination, thereby enhancing the photocatalytic performance of the catalyst. Herein, a series of CdS/g-C_3N_5-X heterojunction catalysts were prepared via an in situ hydrothermal approach. The obtained heterojunction catalysts exhibited a novel coral reef-like morphology which facilitated the exposure of additional active sites, thereby enhancing the adsorption and activation of CO_2. Moreover, studies have shown that CdS can be anchored to the surface of g-C_3N_5 through C-S bonds, forming a built-in electric field at the interface, which accelerated the separation and transfer of photogenerated charges. Consequently, the resulting heterojunction materials demonstrated high efficiency in photocatalytic CO_2 reduction with H_2O as a sacrificial agent. In particular, CdS/g-C_3N_5-0.2 exhibited the maximum photocatalytic performance up to 22.9 $\mu mol \cdot g^{-1} \cdot h^{-1}$, which was 6 times and 3 times that of unmodified g-C_3N_5 and CdS, respectively. The results indicated that the increased active sites and enhanced charge separation of the Cd/g-C_3N_5-0.2 catalyst were the primary reasons for its improved photocatalytic CO_2 reduction performance. This work provides a novel heterojunction-based photocatalyst for efficient CO_2 photocatalytic reduction, offering insights into the preparation of high-performance photocatalysts for sustainable energy applications.

Keywords: carbon nitride; cadmium sulfide; heterojunction; CO_2 reduction; photocatalysis

Academic Editor: Eun Duck Park

Received: 30 December 2024
Revised: 15 January 2025
Accepted: 17 January 2025
Published: 20 January 2025

Citation: Zhang, F.; Xiong, J.; Yu, X.; Wang, L.; Wu, T.; Yu, Z.; Tang, M.; Liu, H.; Chao, Y.; Zhu, W. Coral Reef-like CdS/g-C_3N_5 Heterojunction with Enhanced CO_2 Adsorption for Efficient Photocatalytic CO_2 Reduction. *Catalysts* **2025**, *15*, 94. https://doi.org/10.3390/catal15010094

1. Introduction

In recent years, owing to increasing energy shortages and environmental challenges, solar-driven photocatalytic technologies have garnered widespread attention [1]. Drawing inspiration from photosynthesis in plants, photocatalytic CO_2 conversion using sunlight and H_2O not only helps reduce atmospheric CO_2 concentrations, thereby mitigating the greenhouse effect, but also converts CO_2 into high value chemicals or fuels [2–4]. This is an ideal approach with significant potential. However, several critical challenges persist,

including limited solar energy utilization, rapid recombination of photoexcited charges, and insufficient CO_2 adsorption and activation, which impede the enhancement of photocatalytic CO_2 reduction efficiency [5–7]. Therefore, the rational design of photocatalysts with broad light response, efficient charge separation, and enhanced CO_2 adsorption and activation capabilities are essential to achieving efficient photocatalytic CO_2 reduction.

Since Fujishima and Honda's groundbreaking discovery that TiO_2 electrodes could facilitate photocatalytic water splitting under ultraviolet light [8], numerous semiconductor catalysts have been developed for multiple photocatalytic applications, such as carbon nitrides [9], titanium oxide [10], cadmium sulfide [11], and bismuth tungstate [12]. Among them, carbon nitrides (CNs) have garnered significant attention in various fields, such as gas capture [13], supercapacitors [14], and photocatalysis [15,16], due to their remarkable properties, including affordability, chemical stability, and tunable electronic structures. Compared with the well-studied g-C_3N_4, nitrogen-rich g-C_3N_5, a novel graphite-phase catalyst, exhibits better visible-light absorption [17,18], a higher density of N sites [19], and superior electronic properties [20]. This is attributed to the existence of the N-rich triazole moiety and its extended conjugation [18]. As a result, g-C_3N_5 has been employed in photocatalytic and electrocatalytic hydrogen evolution [21], CO_2 reduction [22], and the degradation of various pollutants [23]. Wang et al. [24] used a simple and environmentally friendly KBr-guided method to create a mesoporous rod-shaped nitrogen-rich graphitic carbon nitride. This unique structure, combined with its high nitrogen content, resulted in a narrow band gap of 1.90 eV, and the generated catalyst demonstrated noticeably better photocatalytic performance. Sadanandan et al. [22] synthesized mesoporous C-doped C_3N_5 through the copolymerization of 3-amino-1,2,4-triazole and trimesic acid using a hard-template method. The resulting material demonstrated enhanced light absorption capacity and increased delocalized π-electron density, leading to excellent photocatalytic CO_2 reduction activity. Nevertheless, g-C_3N_5 suffers from the intrinsic limitation of severe photogenerated charge recombination. To address this, several strategies have been explored, such as incorporating heteroatoms [25,26], coupling with cocatalysts [27,28], and constructing heterojunctions [29,30]. The construction of heterostructures can promotes the spatial separation of photogenerated carriers and maintains the inherent advantages of both catalysts, resulting in superior optical performance compared to individual semiconductors [31–33]. Therefore, an effective strategy for improving the photocatalytic performance of g-C_3N_5 is to select a semiconductor with a compatible energy band structure that can form a heterojunction with g-C_3N_5, thereby suppressing charge recombination. To date, various heterojunction photocatalysts have been extensively explored for their high efficiency in charge separation and transfer. For instance, Li et al. [34] designed and synthesized C_3N_5/Bi_2WO_6 nanocomposites with Z-scheme heterojunctions, achieving effective removal of tetracycline and Cr (VI) from water upon visible light irradiation, which not only promoted charge separation but also retained strong redox potential. Similarly, Wang et al. [35] prepared Z-scheme $LaCoO_3/C_3N_5$ heterojunction photocatalysts using sol–gel and solvothermal methods, significantly enhancing photocatalytic hydrogen production.

Cadmium sulfide (CdS), as a typical reducing semiconductor, possesses excellent visible light absorption properties and an appropriate band gap structure, making it highly active for CO_2 photoreduction [36,37]. However, pristine CdS suffers from severe photoinduced charge recombination and limited photostability [38]. Feng et al. [39] decorated CdS nanocrystals surface with 4-mercaptopyridine (PD) as the unit of a capping ligand using a facile ligand-exchange strategy. CdS-PD nanocrystals demonstrated exceptional performance because the conjugated structure of PD could help photogenerated electrons delocalize in CdS nanocrystals, and N-protonated PD could make it easy to generate a six-membered ring intermediate using CO_2 and water, which can function as the effective

active site for the reduction of CO_2 by photocatalysis. Padervand's group [40] prepared a series of $SnO/CuSnO_3$ heterojunction photocatalytic materials through a single-step hydrothermal method, which not only exhibited excellent performance in photocatalytic dye degradation and carbon dioxide reduction, but also effectively facilitated the alkylation of amines for pharmaceutical applications. Studies have shown that their strong visible light absorption characteristics and high charge separation and transport properties are important factors contributing to their high photocatalytic performance. To address these challenges, we identified that combining g-C_3N_5 with CdS to form a heterojunction offers an effective solution. The heterojunction not only mitigates the inherent drawbacks of both semiconductors but also allows the composite catalyst's energy band structure to facilitate both H_2O oxidation and CO_2 reduction, enabling efficient CO_2 reduction without the need for sacrificial reagents.

In solid–liquid photocatalytic reactions, the adsorption and activation of CO_2 have a significant impact on photocatalytic performance. The morphology of the catalyst significantly influences its ability to absorb and activate CO_2 [41,42]. Regulating the morphology during heterojunction construction can synergistically enhance the photocatalytic CO_2 conversion. For instance, Ijaz et al. [43] synthesized CdV_2O_6/CdS composite via anion exchange, where the abundant active sites and suppressed electron–hole recombination significantly enhanced the photocatalytic efficiency in converting CO_2 into CH_4.

Herein, we prepared a series of CdS/g-C_3N_5-X heterojunction catalysts using an in situ hydrothermal method, resulting in a coral reef-like morphology. CO_2 adsorption isotherms and isosteric heats of adsorption demonstrated that CdS/g-C_3N_5 heterojunction exhibited enhanced CO_2 adsorption activity, primarily due to the more active sites provided by the coral reef-like structure. XPS characterization confirmed the formation of a built-in electric field at the interface of CdS/g-C_3N_5, which promoted the separation and transfer of charges. Among the series of prepared photocatalysts, the CdS/g-C_3N_5-0.2 exhibited significantly higher activity in photocatalytic CO_2 reduction using pure H_2O, achieving performance 6 times that of pristine g-C_3N_5 and 3 times that of CdS.

2. Results and Discussion

The CdS/g-C_3N_5-X (X = 0.05–0.5, where X equals to the mass ratio of CdS to g-C_3N_5) heterojunctions were synthesized using a two-step calcination-hydrothermal method. Among these, CdS/g-C_3N_5-0.2, selected as the benchmark catalyst in this study for its exceptional performance, is hereafter referred to as CdS/g-C_3N_5. The g-C_3N_5 was synthesized via a straightforward thermal polymerization. CdS formation occurred through the reaction between Cd^{2+} ions adsorbed on g-C_3N_5 via strong electrostatic interaction then the sulfide generated by DMSO decomposition at high temperature, resulting in robust interfacial bonding with g-C_3N_5 (Scheme 1) [44]. X-ray diffraction (XRD) was used to confirm the crystal structures of the catalysts. As shown in Figures 1a and S1, the diffraction peaks of the prepared CdS matched those of cubic phase CdS (PDF #97-015-9379). The XRD patterns of CdS/g-C_3N_5-X were essentially consistent with those of pristine CdS and g-C_3N_5, indicating that the crystal structures of both components remained largely unchanged during the recombination process.

A combination of transmission electron microscopy (TEM) and scanning electron microscopy (SEM) methods were used to analyze the morphology and microstructure of the prepared catalysts. In Figure S2, the SEM and TEM images revealed a lamellar morphology for g-C_3N_5 with a smooth surface and a nanoparticle morphology for CdS with a diameter of approximately 200 nm. Notably, the CdS/g-C_3N_5 composite exhibited a distinctive coral reef-like surface (Figure 1b,c), which contrasts with the structures of both g-C_3N_5 and CdS. This observation suggested that the coral reef-like morphology results from the in situ

hydrothermal formation of CdS on the g-C_3N_5 surface. Additionally, CdS/g-C_3N_5-0.05 and CdS/g-C_3N_5-0.1 showed morphology of nanosheets and CdS/g-C_3N_5-0.5 presented a nanoparticle morphology due to the coated CdS (Figure S3). To gain deeper insights into the structure and morphology of CdS/g-C_3N_5, high-resolution transmission electron microscopy (HRTEM) analysis was performed. As depicted in Figure 1d, the HRTEM image of CdS/g-C_3N_5 displayed well-defined lattice fringes, allowing for the identification of crystallographic planes. The lattice spacings of 0.293 and 0.334 nm correspond to the spacing of the (200) and (002) planes of CdS, respectively [45,46]. Moreover, the consistent distribution of C, N, S, and Cd elements on CdS/g-C_3N_5 was shown by elemental mapping images (Figure 1e–i).

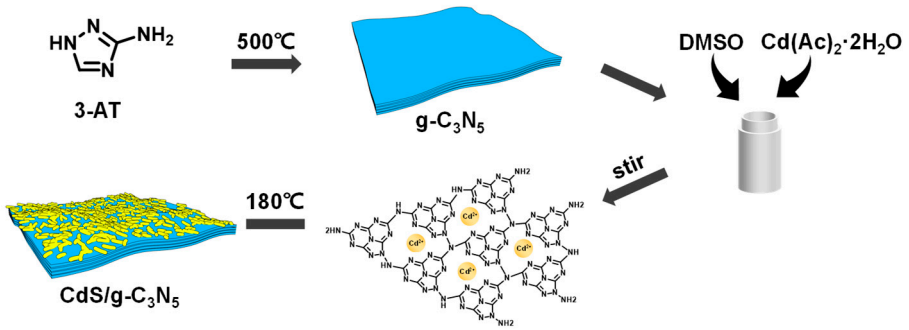

Scheme 1. Synthesis routes of CdS/g-C_3N_5-X.

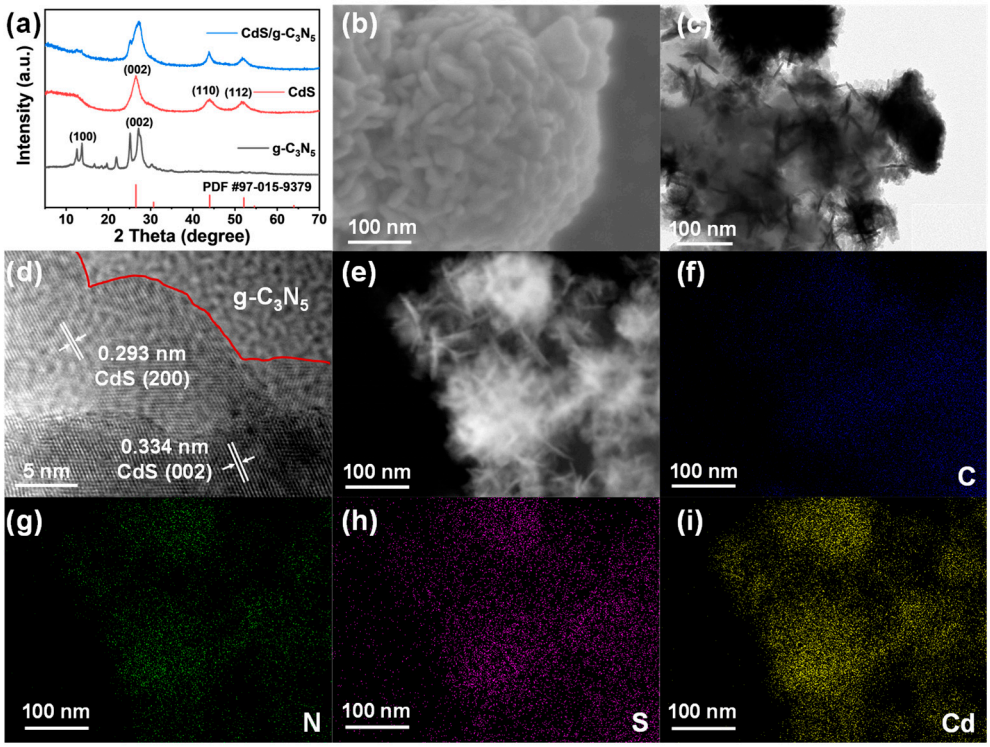

Figure 1. (**a**) XRD patterns of g-C_3N_5, CdS, and CdS/g-C_3N_5, (**b**) SEM, (**c**) TEM, (**d**,**e**) HRTEM, and (**f**–**i**) element mapping images of CdS/g-C_3N_5.

To give an insight into the effects of the coral reef-like morphology on the modification of CdS/g-C_3N_5 heterostructure catalyst, both N_2 adsorption–desorption and CO_2 adsorption isotherms were investigated. As shown in Figure 2a, all N_2 adsorption–desorption isotherms exhibited a H3-type hysteresis loop and IV-type adsorption, clearly confirming the existence of mesopores in the synthesized samples, which matched the pores size

distribution diagram [47] (Figure S4). The specific surface area of CdS/g-C_3N_5 was up to 59.6 m^2/g, significantly exceeding that of pure g-C_3N_5. Although CdS exhibited a slightly higher specific surface area, its proportion in CdS/g-C_3N_5 heterostructure was minimal, which confirmed by the inductively coupled plasma (ICP) results (Table S2). Therefore, the significant increase in specific surface area of CdS/g-C_3N_5 could be attributed to its coral reef-like morphology, which might facilitate CO_2 capture and activation. The CO_2 adsorption capacity of the as-prepared catalysts was measured at 298 K (Figures 2b and S5). As predicted, CdS/g-C_3N_5 displayed the maximum CO_2 adsorption quantity among all samples, reaching 0.39 mmol/g at 1.0 bar which was 3.5 times higher than that of pristine g-C_3N_5. Although the specific surface area of CdS/g-C_3N_5 was smaller than that of CdS, its CO_2 adsorption capacity exceeded that of CdS. Based on the morphology and CO_2 adsorption analyses, we can infer that during the in situ recombination process of the hybrid photocatalyst, the morphology of CdS was reconstructed, leading to increased exposure of edge atoms in the coral reef-like structure, which were more active than the bulk atoms [48,49]. In addition, CdS/g-C_3N_5 demonstrated the largest isosteric adsorption heat, implying the strongest interaction with CO_2 [50] (Figure S6). The aforementioned characterizations revealed that the coral reef-like morphology increased the exposure of active surfaces on the catalyst, thereby enhancing CO_2 adsorption, which is beneficial for photocatalytic CO_2 reduction.

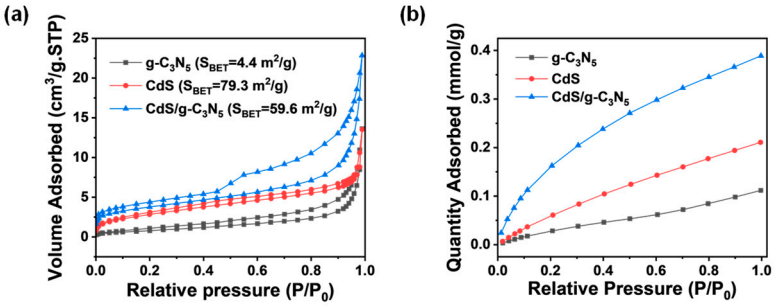

Figure 2. (**a**) N_2 adsorption–desorption isotherms and (**b**) CO_2 adsorption isotherms of the as-prepared samples.

In addition, to confirm the interfacial bonding mode between g-C_3N_5 and CdS, Fourier-transformed infrared spectroscopy (FT-IR) and X-ray photoelectron spectroscopy (XPS) analyses were performed. As depicted in Figure S7, the characteristic peaks observed in the range 3000–3500 cm^{-1}, 1200–1680 cm^{-1}, and around 810 cm^{-1} corresponded to the respective stretching vibrations of -NH_x, aromatic C-N and the out-of-plane bending vibrations of the triazine rings in g-C_3N_5, respectively [51,52]. Notably, the aromatic C-N peak at 1618 cm^{-1} in g-C_3N_5 shifts to 1639 cm^{-1} upon the incorporation of CdS, indicating a strong interaction between the two components, and the same offset also existed in CdS/g-C_3N_5-X (Figure S8). Moreover, XPS measurements were employed to verify the surface chemical composition and chemical states of the catalysts, employing adventitious C1s binding energy (284.8 eV) for calibration. The survey spectrum in Figure S9 revealed that CdS/g-C_3N_5 was primarily composed of C, N, S and Cd element, indicating that g-C_3N_5 and CdS coexist in the CdS/g-C_3N_5 heterojunction catalyst, which was consistent with the EDX consequences. Figure 3a showed the C 1s peak in the XPS spectra, where the peak centered at approximately 288.1 eV corresponded to N=C-N in triazine skeleton of g-C_3N_5 [15]. In the C 1s XPS spectrum of CdS/g-C_3N_5, a new peak at 287.0 eV was observed, which was ascribed to carbon in the C-S bonds [53,54]. This assignment was further supported by the corresponding S 2p spectra (Figure 3c). Additionally, the Cd 3d spectra (Figure 3d) indicated the presence of Cd $3d_{5/2}$ and Cd $3d_{3/2}$, and the binding energy of both Cd $3d_{5/2}$ and Cd $3d_{3/2}$ had a negative shift by 0.1 eV after combining with g-C_3N_5.

Interestingly, the N 1s binding energy of CdS/g-C_3N_5 shifted to a higher binding energy by 0.1 eV in comparison with that of g-C_3N_5 (Figure 3b). Accordingly, it was suggested that g-C_3N_5 might be linked to CdS via C-S bonds, with g-C_3N_5 acting as an electron donor when forming a heterostructure with CdS. The FT-IR and XPS analyses revealed a significant interaction between the two components and confirmed the successful construction of a built-in electric field in the CdS/g-C_3N_5 heterojunction catalyst [45].

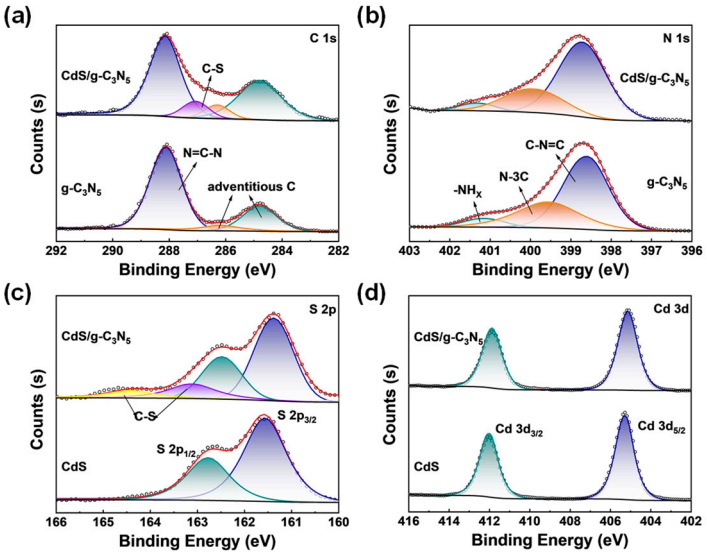

Figure 3. High-resolution XPS spectra of (**a**) C 1s, (**b**) N 1s, (**c**) S 2p, and (**d**) Cd 3d for the as-prepared specimens.

The band structure of the as-prepared photocatalysts were measured using ultraviolet-visible diffuse reflectance spectroscopy (UV−Vis DRS) and Mott–Schottky (MS) measurement to evaluate their potential applications in photocatalytic CO_2 reduction. As displayed in Figure 4a, all the catalysts exhibited broad absorption in both UV and visible regions, with absorption edge at 670, 530, and 580 nm, for g-C_3N_5, CdS, and CdS/g-C_3N_5, respectively. Compared with g-C_3N_4, which has a light absorption edge of 470 nm [55], CdS/g-C_3N_5 exhibited a stronger capability to absorb visible light. This improvement could be ascribed to the superior light absorption characteristics of g-C_3N_5. On the basis of the Tauc plots, the band gap values of the as-prepared photocatalysts estimated from UV-Vis DRS were to be 2.26, 2.44, and 2.40 eV for g-C_3N_5, CdS, and CdS/g-C_3N_5, respectively (Figure S10). Furthermore, in order to determine the positions of the conduction band (CB) for the photocatalysts, MS measurements were performed by varying the frequency of the alternating current, for which the flat band positions were determined to be −1.41, −1.68 and −1.32 V for g-C_3N_5, CdS, and CdS/g-C_3N_5, respectively, approximately corresponding to the bottom of the CB for n-type semiconductors (Figure S11). The relative electronic band structures of as-prepared photocatalysts were shown in Figure 4b, indicating that the obtained photocatalysts has thermodynamically satisfied the simultaneous photoreduction of CO_2 and the photooxidation of H_2O [56].

To further investigate the improvement of catalytic activity resulting from the construction of heterojunction, the separation and transfer performances of photo-induced carriers for obtained photocatalysts were evaluated using steady-state photoluminescence (PL) spectra, time-resolved PL (tr-PL) spectra, transient photocurrent (TPC) responses, and electrochemical impedance spectra (EIS). As is well known, PL spectra is an extensively used photophysical measurement to monitor the transfer dynamics of photo-generated carriers [57]. As observed in Figure 4c, CdS/g-C_3N_5 exhibited a smaller intensity of PL emission compared with g-C_3N_5, indicating that the construction of the heterostructure significantly

reduced the recombination of photo-generated electron–hole pairs, which could promote the separation of photo-generated carriers. In addition, tr-PL spectra (Figure 4d) indicated that the average photoluminescence lifetimes were in the order of g-C_3N_5 > CdS/g-C_3N_5, suggesting that the construction of heterostructures in CdS/g-C_3N_5 facilitates the participation of photo-generated electrons or holes in surface photoredox reactions [58], which can enhance their photocatalytic efficiency. The TPC responses (Figure 4e) of the obtained photocatalysts demonstrated that, compared to g-C_3N_5, CdS/g-C_3N_5 exhibited a higher and more stable photocurrent under cyclic light on/off conditions. The EIS data were collected to assess the charge-transfer resistances of the as-prepared photocatalysts. In general, a smaller radius typically indicates higher charge transfer efficiency of photo-generated carriers. As shown in Figure 4f, CdS/g-C_3N_5 exhibited a smaller radius on the Nyquist plot, showing that CdS/g-C_3N_5 has the highest charge transfer efficiency. To sum up, the constructed CdS/g-C_3N_5 heterojunction revealed efficient carrier transfer and separation, which could lead to higher photocatalytic efficiency.

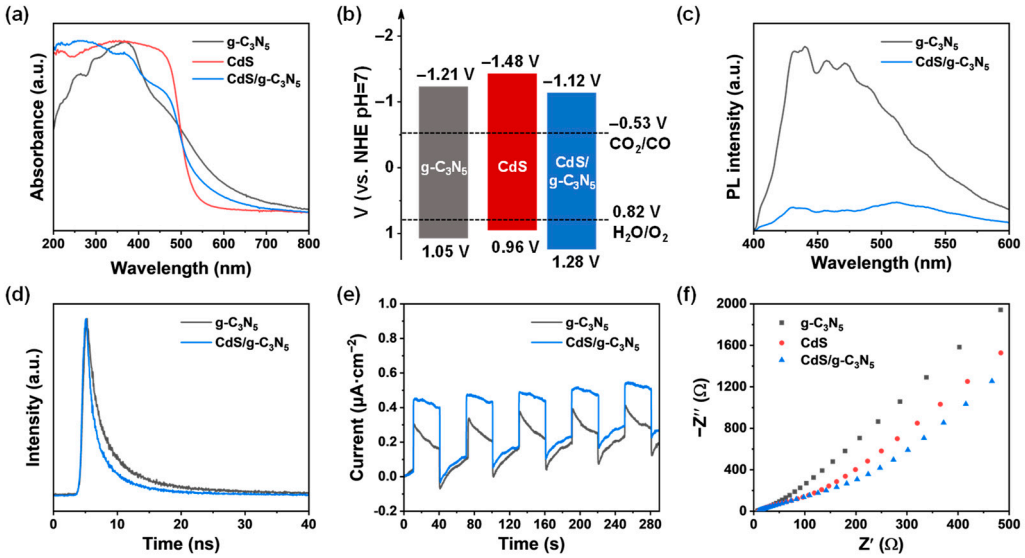

Figure 4. (**a**) UV–Vis DRS and (**b**) band structures of g-C_3N_5, CdS, and CdS/g-C_3N_5, (**c**) PL spectra, (**d**) tr-PL spectra, and (**e**) TPC responses of g-C_3N_5 and CdS/g-C_3N_5, (**f**) EIS plots of g-C_3N_5, CdS, and CdS/g-C_3N_5.

Encouraged by the excellent CO_2 capture capacity, suitable energy band structures, and fast separation and transfer efficiencies of photo-induced carriers, g-C_3N_5, CdS, and CdS/g-C_3N_5-X were evaluated for their photocatalytic efficiency to CO_2 reduction with H_2O as the hole scavenge under ambient conditions and UV-Vis light irradiation without any photosensitizer. From Figure 5a, it was indicated all the obtained photocatalysts can realize the photoreduction of CO_2 to CO as the main product with a small amount of CH_4 confirmed by the GC spectra. As expected, compared with g-C_3N_5 or CdS, CdS/g-C_3N_5-X showed the better performance. Notably, CdS/g-C_3N_5-0.2 exhibited the highest performance, affording CO with a production rate of 22.9 $\mu mol \cdot g^{-1} \cdot h^{-1}$, which is 3 times that of CdS and 6 times that of g-C_3N_5, and even surpasses the performance of g-C_3N_4 (2.38 $\mu mol \cdot g^{-1} \cdot h^{-1}$) and CdS/g-$C_3N_4$-0.2 (6.29 $\mu mol \cdot g^{-1} \cdot h^{-1}$). This was in strong agreement with its superior CO_2 capture capacity and enhanced charge carrier transfer efficiency. Furthermore, by comparing with some similar works, this work has a better performance for CO production (Table S3). To evaluate the stability of the catalysts, recycling tests of CdS/g-C_3N_5-0.2 were conducted. The results demonstrated that the CO production rate remained consistently stable after five consecutive reuse cycles (Figure 5b). In addition, a comparison of the SEM, XRD, FT-IR, and UV-Vis DRS results of CdS/g-C_3N_5-0.2 before

and after the cycling tests (Figures S12–S15) revealed no significant variations indicating that the catalyst maintained robust structural and chemical solidness.

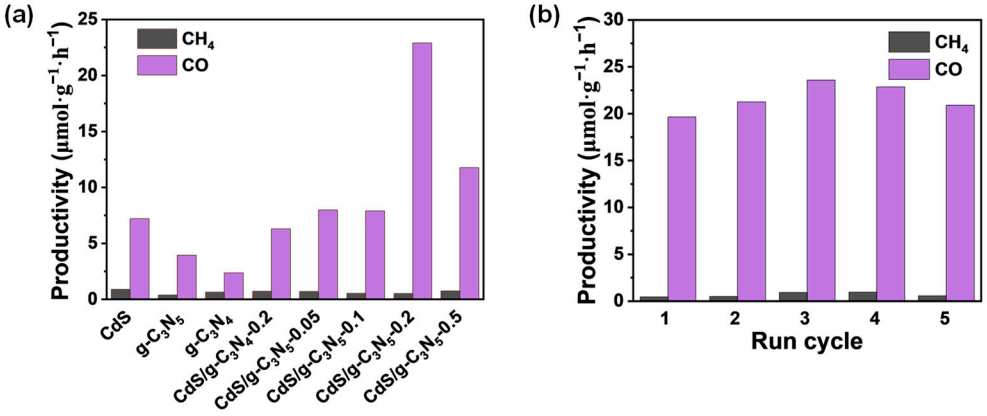

Figure 5. (**a**) Average productivity of CO and CH_4 over the as-prepared samples, (**b**) recyclability test of CdS/g-C_3N_5-0.2.

3. Materials and Methods

3.1. Materials and Chemicals

All chemicals were utilized as received, without additional purification. The 3-Amino-1,2,4-triazole (3-AT) was obtained from Bidepharm (Shanghai, China). Dimethyl sulfoxide (DMSO) was sourced from Aladdin (Shanghai, China). Cadmium (II) acetate dihydrate ($Cd(Ac)_2{\cdot}2H_2O$) and Nafion were purchased from Damas-Beta (Shanghai, China). Sodium sulfate (Na_2SO_4) and dicyandiamide (DCDA) were supplied by Tokyo Chemical Industry (Tokyo, Japan) and Innochem (Beijing, China), respectively. Throughout this work, Milli-Q water (MilliporeSigma, Burlington, MA, USA, 18 MΩ·cm) was used whenever applicable.

3.2. Preparation of g-C_3N_5

The g-C_3N_5 was prepared via a straightforward thermal polymerization method. Typically, 2 g of 3-AT was placed into a covered corundum crucible, which was transferred to a muffle furnace. At a rate of 5 °C/min, the sample was heated to 500 °C and held for 3 h. Then, the resulting product was collected and finely grounded using an agate mortar, and the C/N ratio was found to be about 4.7 by organic element analysis (Table S1).

3.3. Preparation of g-C_3N_4

Typically, a corundum crucible containing 2 g of DCDA was directly calcined at 550 °C for 3 h with a heating rate of 5 °C/min in air. The resulting product was collected and finely grounded using an agate mortar.

3.4. Preparation of CdS/g-C_3N_5-X

73.8 mg of $Cd(Ac)_2{\cdot}2H_2O$ and 200 mg of the prepared g-C_3N_5 were scattered in 20 mL of DMSO with stirring for 30 min. After that, the suspension was put in an autoclave lined with polytetrafluoroethylene and heated to 180 °C for 12 h. The product was allowed to cool to room temperature, then isolated through three cycles of centrifugation and redispersion in ethanol and water. Eventually, the resulting powder was vacuum-dried for 12 h at 60 °C. By varying the mass ratio of CdS to g-C_3N_5 in the range of 0.05–0.5, a series of CdS/g-C_3N_5-X nanocomposites were obtained through the same method.

3.5. Preparation of CdS/g-C_3N_4-0.2

The CdS/g-C_3N_4-0.2 was synthesized following the same synthetic procedure to that of CdS/g-C_3N_5-0.2, except for the addition of g-C_3N_4 (200 mg) instead of g-C_3N_5 (200 mg).

3.6. Characterization of Catalysts

The SEM images were acquired using Hitachi SU8010 Cold-Field Emission SEM (Hitachi, Tokyo, Japan) with an accelerating voltage at 5 kV. TEM images were captured on a JEOL JEM 1200EX electron microscope (JEOL Ltd., Tokyo, Japan) operating at an accelerating voltage of 100 kV. HRTEM and energy dispersive X-ray (EDX) mapping images were collected using a FEI Tecnai G2 F30 S-TWIN microscopy (Thermo Fisher Scientific, Waltham, MA, USA) with an accelerating voltage of 300 kV. XRD patterns were documented on a Bruker D8 Focus diffractometer (Bruker, Billerica, MA, USA) operating at 40 kV and 40 mA, with scanning diffraction angles from 5° to 90°. FT-IR spectra were obtained on a Bruker INVENIO-S spectrophotometer (Bruker, Billerica, MA, USA)with samples were dispersed in KBr. XPS spectra were measured using a Thermo escalab 250Xi electron spectrometer (Thermo Fisher Scientific, Waltham, MA, USA). UV-Vis DRS were recorded by a Shimadzu UV-3600 UV-Vis spectrometer (Shimadzu, Kyoto, Japan). The PL measurements were conducted using a NanoLOG-TCSPC luminescence spectrophotometer (HORIBA, Kyoto, Japan) with an excitation wavelength of 360 nm. Surface area and pore size distributions were analyzed using N_2 adsorption–desorption isotherm on a Quantachrome Autosorb-iQ3 surface area and porosimetry analyzer. CO_2 adsorption curves were measured using a BSD 660M A6B3M surface analyzer (Best Instrument Technology Co., Ltd, Beijing, China).

3.7. Photoelectrochemical Measurements

The TPC responses, EIS Nyquist plots, and MS plots were executed in a 0.5 M Na_2SO_4 solution using a Gamry Interface1010 electrochemical workstation (Gamry Instruments Inc., Warminster, PA, USA) with a standard three-electrode system, while a Pt mesh and an Ag/AgCl electrode functioned as the counter and reference electrodes, respectively. The working electrode was an indium tin oxide (ITO) glass coated with the photocatalyst. Initially, the ITO glass underwent thorough cleaning via ultrasonic treatment in ethanol for 30 min. Subsequently, 10 mg of the photocatalyst was dispersing in 1 mL of ethanol, followed by the addition of 20 μL of Nafion to form a suspension. The mixture was sonicated for 1 h to ensure homogeneity. Subsequently, the prepared suspension was carefully dropped onto the center of a ~1 cm^2 ITO substrate and dried at room temperature.

3.8. Photocatalytic Activity Evaluation

The photocatalytic activity evaluation were conducted in a sealed 250 mL glass reactor under UV-Vis light illumination. A 300 W xenon (Xe) lamp (CEL-HXF300-T3, Ceaulight, Beijing China Education Au-light Co., Ltd., Beijing, China) was used as the light source, positioned above the reactor. Typically, 2 mg of photocatalyst was scattered in the 10 mL of H_2O and subjected to thorough ultrasonication. Prior to radiation exposure, the reactor was purged with pure CO_2 for 30 min to ensure a CO_2-saturated environment. The reactor temperature was maintained at room ambient conditions using a cooling water circulator. Product distribution was analyzed using gas chromatography (GC-9790 II, Fuli, Wenling, China). Methane (CH_4) was identified using a flame ionization detector (FID), while carbon monoxide (CO) was converted to CH_4 by a methanation reactor and subsequently analyzed by the FID.

4. Conclusions

The CdS/g-C_3N_5 heterojunction catalyst was synthesized using a straightforward calcination-hydrothermal two-step method, enabling strong interfacial interaction between CdS and g-C_3N_5. Notably, an unique coral reef-like morphology was formed, enhancing the CO_2 adsorption capability of the CdS/g-C_3N_5 heterojunction catalyst. Moreover, the heterojunction construction between CdS and g-C_3N_5 induced the formation of the built-

in electric field, facilitating efficient charge separation and transfer. On account of the synergistic effects of enhanced CO_2 adsorption and efficient charge separation and transfer capabilities, the CdS/g-C_3N_5 heterojunction catalyst showed the superior performance for photocatalytic of CO_2, affording CO with a production rate of 22.9 $\mu mol \cdot g^{-1} \cdot h^{-1}$ using water as the oxidant, representing a trifold increase compared to CdS and a sixfold increase compared to g-C_3N_5. This work provides new insights into the design and fabrication of photocatalytically active heterojunctions with high efficiency for solar energy conversion.

Supplementary Materials: The following supporting information can be downloaded at: https://www.mdpi.com/article/10.3390/catal15010094/s1, Figure S1: XRD patterns of CdS/g-C_3N_5-0.05, CdS/g-C_3N_5-0.1 and CdS/g-C_3N_5-0.5; Figure S2: SEM images of (a) g-C_3N_5 and (b) CdS, TEM images of (c) g-C_3N_5, (d) CdS; Figure S3: SEM images of (a) CdS/g-C_3N_5-0.05, (b) CdS/g-C_3N_5-0.1 and (c) CdS/g-C_3N_5-0.5; Figure S4: BJH pore size distribution plot of prepared catalysts; Figure S5: CO_2 adsorption isotherms of CdS/g-C_3N_5-0.05, CdS/g-C_3N_5-0.1 and CdS/g-C_3N_5-0.5; Figure S6: Isosteric heats of adsorption (Qst) for CO_2 by different samples; Figure S7: FT-IR spectra of g-C_3N_5 and CdS/g-C_3N_5; Figure S8: FT-IR spectra of g-C_3N_5, CdS/g-C_3N_5-0.05, CdS/g-C_3N_5-0.1 and CdS/g-C_3N_5-0.5; Figure S9: XPS survey spectrum of CdS/g-C_3N_5; Figure S10: Tauc plots of g-C_3N_5, CdS, and CdS/g-C_3N_5; Figure S11: Flat potential of (a) g-C_3N_5, (b) CdS, and (c) CdS/g-C_3N_5 determined by MS measurement; Figure S12: SEM images of CdS/g-C_3N_5-0.2 (a) before and (b) after use; Figure S13: FT-IR spectra of CdS/g-C_3N_5-0.2 before and after use; Figure S14: XRD patterns of CdS/g-C_3N_5-0.2 before and after use; Figure S15: UV-Vis DRS of CdS/g-C_3N_5-0.2 before and after use; Table S1: C and N contents of g-C_3N_5 obtained by elemental analysis; Table S2: Cd content of CdS/g-C_3N_5-0.2 obtained by ICP analysis; Table S3: Comparative analysis of the catalyst with similar catalysts. Refs. [59–62] are cited in the Supplementary Materials.

Author Contributions: F.Z.: synthesis, methodology, formal analysis, data curation, visualization, writing—original draft preparation; J.X. and L.W.: characterization studies; X.Y.: investigation, writing—review and editing project administration, funding acquisition; T.W.: formal analysis; Z.Y. and M.T.: review and editing; H.L.: resources; Y.C. and W.Z.: conceptualization, resources, funding acquisition, supervision, writing—review and editing. All authors have read and agreed to the published version of the manuscript.

Funding: This work was supported by the Beijing Municipal Natural Science Foundation (2244076), China National Funds for Distinguished Young Scientists (22425808), the Science Foundation of China University of Petroleum, Beijing (2462023QNXZ009), 1158 Project (SKLHOP2024115804) and the School of Chemistry and Chemical Engineering, Henan Normal University.

Data Availability Statement: All data are present within the manuscript.

Conflicts of Interest: The authors declare no conflicts of interest.

References

1. Fang, S.; Rahaman, M.; Bharti, J.; Reisner, E.; Robert, M.; Ozin, G.A.; Hu, Y.H. Photocatalytic CO_2 Reduction. *Nat. Rev. Methods Primers* **2023**, *3*, 61. [CrossRef]
2. Chi, X.; Lan, Z.; Chen, Q.; Zhang, X.; Chen, X.; Zhang, G.; Wang, X. Electronic Transmission Channels Promoting Charge Separation of Conjugated Polymers for Photocatalytic CO_2 Reduction with Controllable Selectivity. *Angew. Chem. Int. Ed.* **2023**, *62*, e202303785. [CrossRef]
3. Liu, D.; Jiang, L.; Chen, D.; Hao, Z.; Deng, B.; Sun, Y.; Liu, X.; Jia, B.; Chen, L.; Liu, H. Twin S-Scheme g-C_3N_4/$CuFe_2O_4$/$ZnIn_2S_4$ Heterojunction with a Self-Supporting Three-Phase System for Photocatalytic CO_2 Reduction: Mechanism Insight and DFT Calculations. *ACS Catal.* **2024**, *14*, 5326–5343. [CrossRef]
4. Wang, W.; Deng, C.; Xie, S.; Li, Y.; Zhang, W.; Sheng, H.; Chen, C.; Zhao, J. Photocatalytic C–C Coupling from Carbon Dioxide Reduction on Copper Oxide with Mixed-Valence Copper(I)/Copper(II). *J. Am. Chem. Soc.* **2021**, *143*, 2984–2993. [CrossRef]
5. Xu, Q.; Xia, Z.; Zhang, J.; Wei, Z.; Guo, Q.; Jin, H.; Tang, H.; Li, S.; Pan, X.; Su, Z.; et al. Recent Advances in Solar-driven CO_2 Reduction over g-C_3N_4-based Photocatalysts. *Carbon Energy* **2023**, *5*, e205. [CrossRef]

6. Duan, Y.; Wang, Y.; Zhang, W.; Zhang, J.; Ban, C.; Yu, D.; Zhou, K.; Tang, J.; Zhang, X.; Han, X.; et al. Simultaneous CO_2 and H_2O Activation via Integrated Cu Single Atom and N Vacancy Dual-Site for Enhanced CO Photo-Production. *Adv. Funct. Mater.* **2023**, *33*, 2301729. [CrossRef]
7. Li, M.; Wu, S.; Liu, D.; Ye, Z.; Wang, L.; Kan, M.; Ye, Z.; Khan, M.; Zhang, J. Engineering Spatially Adjacent Redox Sites with Synergistic Spin Polarization Effect to Boost Photocatalytic CO_2 Methanation. *J. Am. Chem. Soc.* **2024**, *146*, 15538–15548. [CrossRef]
8. Fujishima, A.; Honda, K. Electrochemical Photolysis of Water at a Semiconductor Electrode. *Nature* **1972**, *238*, 37–38. [CrossRef]
9. Fu, J.; Yu, J.; Jiang, C.; Cheng, B. g-C_3N_4-Based Heterostructured Photocatalysts. *Adv. Energy Mater.* **2018**, *8*, 1701503. [CrossRef]
10. Guo, Q.; Zhou, C.; Ma, Z.; Yang, X. Fundamentals of TiO_2 Photocatalysis: Concepts, Mechanisms, and Challenges. *Adv. Mater.* **2019**, *31*, 1901997. [CrossRef] [PubMed]
11. Bie, C.; Zhu, B.; Xu, F.; Zhang, L.; Yu, J. In Situ Grown Monolayer N-Doped Graphene on CdS Hollow Spheres with Seamless Contact for Photocatalytic CO_2 Reduction. *Adv. Mater.* **2019**, *31*, 1902868. [CrossRef] [PubMed]
12. Chen, T.; Liu, L.; Hu, C.; Huang, H. Recent Advances on Bi_2WO_6-Based Photocatalysts for Environmental and Energy Applications. *Chin. J. Catal.* **2021**, *42*, 1413–1438. [CrossRef]
13. Tabarkhoon, F.; Abolghasemi, H.; Rashidi, A.; Bazmi, M.; Alivand, M.S.; Tabarkhoon, F.; Farahani, M.V.; Esrafili, M.D. Synthesis of Novel and Tunable Micro-Mesoporous Carbon Nitrides for Ultra-High CO_2 and H_2S Capture. *Chem. Eng. J.* **2023**, *456*, 140973. [CrossRef]
14. Yang, W.; Hou, L.; Xu, X.; Li, Z.; Ma, X.; Yang, F.; Li, Y. Carbon Nitride Template-Directed Fabrication of Nitrogen-Rich Porous Graphene-like Carbon for High Performance Supercapacitors. *Carbon* **2018**, *130*, 325–332. [CrossRef]
15. Zhang, J.; Li, Z.; He, J.; Tao, H.; Chen, M.; Zhou, Y.; Zhu, M. Reinforced Photogenerated Electrons in Few-Layer C_3N_5 for Enhanced Catalytic NO Oxidation and CO_2 Reduction. *ACS Catal.* **2023**, *13*, 785–795. [CrossRef]
16. Wang, H.; Jiang, J.; Yu, L.; Peng, J.; Song, Z.; Xiong, Z.; Li, N.; Xiang, K.; Zou, J.; Hsu, J.; et al. Tailoring Advanced N-Defective and S-Doped g-C_3N_4 for Photocatalytic H_2 Evolution. *Small* **2023**, *19*, 2301116. [CrossRef]
17. Kumar, P.; Vahidzadeh, E.; Thakur, U.K.; Kar, P.; Alam, K.M.; Goswami, A.; Mahdi, N.; Cui, K.; Bernard, G.M.; Michaelis, V.K.; et al. C_3N_5: A Low Bandgap Semiconductor Containing an Azo-Linked Carbon Nitride Framework for Photocatalytic, Photovoltaic and Adsorbent Applications. *J. Am. Chem. Soc.* **2019**, *141*, 5415–5436. [CrossRef]
18. Mane, G.P.; Talapaneni, S.N.; Lakhi, K.S.; Ilbeygi, H.; Ravon, U.; Al-Bahily, K.; Mori, T.; Park, D.; Vinu, A. Highly Ordered Nitrogen-Rich Mesoporous Carbon Nitrides and Their Superior Performance for Sensing and Photocatalytic Hydrogen Generation. *Angew. Chem. Int. Ed.* **2017**, *56*, 8481–8485. [CrossRef] [PubMed]
19. Wang, Y.; Ngoc Pham, T.; Tian, Y.; Morikawa, Y.; Yan, L. Density Functional Theory Study on a Nitrogen-Rich Carbon Nitride Material C_3N_5 as Photocatalyst for CO_2 Reduction to C1 and C2 Products. *J. Colloid Interface Sci.* **2021**, *585*, 740–749. [CrossRef]
20. Ng, S.-F.; Foo, J.J.; Ong, W.-J. Isotype Heterojunction: Tuning the Heptazine/Triazine Phase of Crystalline Nitrogen-Rich C_3N_5 towards Multifunctional Photocatalytic Applications. *Mater. Horiz.* **2024**, *11*, 408–418. [CrossRef]
21. Bu, X.; Liang, X.; Bu, Y.; Quan, Q.; Meng, Y.; Lai, Z.; Wang, W.; Liu, C.; Lu, J.; Lawrence Wu, C.-M.; et al. NiMo@C_3N_5 Heterostructures with Multiple Electronic Transmission Channels for Highly Efficient Hydrogen Evolution from Alkaline Electrolytes and Seawater. *Chem. Eng. J.* **2022**, *438*, 135379. [CrossRef]
22. Sadanandan, A.M.; Fawaz, M.; Dharmarajan, N.P.; Huš, M.; Singh, G.; Sathish, C.; Likozar, B.; Li, Z.; Ruban, A.M.; Jeon, C.-H.; et al. Mesoporous C-Doped C_3N_5 as a Superior Photocatalyst for CO_2 Reduction. *Appl. Catal. B-Environ.* **2025**, *362*, 124701. [CrossRef]
23. Cai, Z.; Huang, Y.; Ji, H.; Liu, W.; Fu, J.; Sun, X. Type-II Surface Heterojunction of Bismuth-Rich $Bi_4O_5Br_2$ on Nitrogen-Rich g-C_3N_5 Nanosheets for Efficient Photocatalytic Degradation of Antibiotics. *Sep. Purif. Technol.* **2022**, *280*, 119772. [CrossRef]
24. Wang, H.; Li, M.; Lu, Q.; Cen, Y.; Zhang, Y.; Yao, S. A Mesoporous Rod-like g-C_3N_5 Synthesized by Salt-Guided Strategy: As a Superior Photocatalyst for Degradation of Organic Pollutant. *ACS Sustain. Chem. Eng.* **2019**, *7*, 625–631. [CrossRef]
25. Li, K.; Cai, W.; Zhang, Z.; Xie, H.; Zhong, Q.; Qu, H. Boron Doped C_3N_5 for Photocatalytic Nitrogen Fixation to Ammonia: The Key Role of Boron in Nitrogen Activation and Mechanism. *Chem. Eng. J.* **2022**, *435*, 135017. [CrossRef]
26. Hu, C.; Lin, Y.-H.; Yoshida, M.; Ashimura, S. Influence of Phosphorus Doping on Triazole-Based g-C_3N_5 Nanosheets for Enhanced Photoelectrochemical and Photocatalytic Performance. *ACS Appl. Mater. Interfaces* **2021**, *13*, 24907–24915. [CrossRef]
27. Cui, E.; Lu, Y.; Li, Z.; Sang, J.; Wang, Z.; Xie, M.; Yang, X.; Cao, J.; Zhang, Y. Unveiling the Charge Transfer Dynamics Regulated by Bonding Evolution in Single-Atom Pt/C_3N_5 for Boosting Hydrogen Evolution. *Appl. Catal. B-Environ.* **2024**, *347*, 123806. [CrossRef]
28. Liu, Q.; Du, X.; Zhou, A.; Chen, J.; Wang, X.; Wang, R.; Cheng, M.; Hu, J.; Wei, T.; Cui, Y.; et al. Dipole Field as Charge-Transfer Bridge between Cu Atomic Clusters/PtCu Alloy Nanocubes and Nitrogen-Rich C_3N_5 for Superior Photocatalytic Hydrogen Evolution. *J. Colloid Interface Sci.* **2025**, *678*, 114–124. [CrossRef]
29. Li, Q.; Song, S.; Mo, Z.; Zhang, L.; Qian, Y.; Ge, C. Hollow Carbon Nanospheres@graphitic C_3N_5 Heterostructures for Enhanced Oxygen Electroreduction. *Appl. Surf. Sci.* **2022**, *579*, 152006. [CrossRef]

30. Yin, H.; Cao, Y.; Fan, T.; Zhang, M.; Yao, J.; Li, P.; Chen, S.; Liu, X. In Situ Synthesis of Ag_3PO_4/C_3N_5 Z-Scheme Heterojunctions with Enhanced Visible-Light-Responsive Photocatalytic Performance for Antibiotics Removal. *Sci. Total Environ.* **2021**, *754*, 141926. [CrossRef] [PubMed]
31. Li, X.; Garlisi, C.; Guan, Q.; Anwer, S.; Al-Ali, K.; Palmisano, G.; Zheng, L. A Review of Material Aspects in Developing Direct Z-Scheme Photocatalysts. *Mater. Today* **2021**, *47*, 75–107. [CrossRef]
32. Li, X.; Sun, H.; Xie, Y.; Liang, Y.; Gong, X.; Qin, P.; Jiang, L.; Guo, J.; Liu, C.; Wu, Z. Principles, Synthesis and Applications of Dual Z-Scheme Photocatalysts. *Coord. Chem. Rev.* **2022**, *467*, 214596. [CrossRef]
33. Nasir, J.A.; Munir, A.; Ahmad, N.; Rehman, Z. Photocatalytic Z-Scheme Overall Water Splitting: Recent Advances in Theory and Experiments. *Adv. Mater.* **2021**, *33*, 2105195. [CrossRef] [PubMed]
34. Li, S.; Cai, M.; Liu, Y.; Zhang, J.; Wang, C.; Zang, S.; Li, Y.; Zhang, P.; Li, X. In Situ Construction of a C_3N_5 Nanosheet/Bi_2WO_6 Nanodot S-Scheme Heterojunction with Enhanced Structural Defects for the Efficient Photocatalytic Removal of Tetracycline and Cr(VI). *Inorg. Chem. Front.* **2022**, *9*, 2479–2497. [CrossRef]
35. Wang, R.; Zhang, K.; Zhong, X.; Jiang, F. Z-Scheme $LaCoO_3/C_3N_5$ for Efficient Full-Spectrum Light-Simulated Solar Photocatalytic Hydrogen Generation. *RSC Adv.* **2022**, *12*, 24026–24036. [CrossRef]
36. Cheng, L.; Xiang, Q.; Liao, Y.; Zhang, H. CdS-Based Photocatalysts. *Energy Environ. Sci.* **2018**, *11*, 1362–1391. [CrossRef]
37. Zhu, C.; Liu, C.; Fu, Y.; Gao, J.; Huang, H.; Liu, Y.; Kang, Z. Construction of CDs/CdS Photocatalysts for Stable and Efficient Hydrogen Production in Water and Seawater. *Appl. Catal. B-Environ.* **2019**, *242*, 178–185. [CrossRef]
38. Nasir, J.A.; Rehman, Z.U.; Shah, S.N.A.; Khan, A.; Butler, I.S.; Catlow, C.R.A. Recent Developments and Perspectives in CdS-Based Photocatalysts for Water Splitting. *J. Mater. Chem. A* **2020**, *8*, 20752–20780. [CrossRef]
39. Feng, Y.-X.; Wang, H.-J.; Wang, J.-W.; Zhang, W.; Zhang, M.; Lu, T.-B. Stand-Alone CdS Nanocrystals for Photocatalytic CO_2 Reduction with High Efficiency and Selectivity. *ACS Appl. Mater. Interfaces* **2021**, *13*, 26573–26580. [CrossRef]
40. Padervand, M.; Bargahi, A.; Eftekhari-Sis, B.; Saadi, M.; Ghasemi, S.; Dawi, E.A.; Labidi, A.; Mahmoudi, G.; Servati Gargari, M. In-Situ Synthesis of SnO/$CuSnO_3$ Nanostructures to Catalyze Azo Dye Degradation, CO_2 Reduction, and Amines Direct Alkylation Reactions under Visible Light. *Results Eng.* **2024**, *23*, 102515. [CrossRef]
41. He, Y.; Yin, L.; Yuan, N.; Zhang, G. Adsorption and Activation, Active Site and Reaction Pathway of Photocatalytic CO_2 Reduction: A Review. *Chem. Eng. J.* **2024**, *481*, 148754. [CrossRef]
42. Singh, S.; Punia, R.; Pant, K.K.; Biswas, P. Effect of Work-Function and Morphology of Heterostructure Components on CO_2 Reduction Photo-Catalytic Activity of MoS_2-Cu_2O Heterostructure. *Chem. Eng. J.* **2022**, *433*, 132709. [CrossRef]
43. Ijaz, S.; Ehsan, M.F.; Ashiq, M.N.; Karamt, N.; Najam-ul-Haq, M.; He, T. Flower-like CdS/CdV_2O_6 Composite for Visible-Light Photoconversion of CO_2 into CH_4. *Mater. Des.* **2016**, *107*, 178–186. [CrossRef]
44. Wang, M.; Chen, D.; Li, N.; Xu, Q.; Li, H.; He, J.; Lu, J. Ni–Co Bimetallic Hydroxide Nanosheet Arrays Anchored on Graphene for Adsorption-Induced Enhanced Photocatalytic CO_2 Reduction. *Adv. Mater.* **2022**, *34*, 2202960. [CrossRef]
45. Li, R.; Li, H.; Zhang, X.; Liu, B.; Wu, B.; Zhu, B.; Yu, J.; Liu, G.; Zheng, L.; Zeng, Q. S-Scheme g-C_3N_4/CdS Heterostructures Grafting Single Pd Atoms for Ultrafast Charge Transport and Efficient Visible-Light-Driven H_2 Evolution. *Adv. Funct. Mater.* **2024**, *34*, 2402797. [CrossRef]
46. Wang, S.; Yu, J.; Zhao, P.; Guo, S.; Han, S. One-Step Synthesis of Water-Soluble CdS Quantum Dots for Silver-Ion Detection. *ACS Omega* **2021**, *6*, 7139–7146. [CrossRef] [PubMed]
47. Balakrishnan, M.; John, R. Impact of Ni Metal Ion Concentration in TiO_2 Nanoparticles for Enhanced Photovoltaic Performance of Dye Sensitized Solar Cell. *J. Mater. Sci. Mater. Electron.* **2021**, *32*, 5295–5308. [CrossRef]
48. Wang, F.; Hou, T.; Zhao, X.; Yao, W.; Fang, R.; Shen, K.; Li, Y. Ordered Macroporous Carbonous Frameworks Implanted with CdS Quantum Dots for Efficient Photocatalytic CO_2 Reduction. *Adv. Mater.* **2021**, *33*, 2102690. [CrossRef]
49. Wang, N.; Cheong, S.; Yoon, D.-E.; Lu, P.; Lee, H.; Lee, Y.K.; Park, Y.-S.; Lee, D.C. Efficient, Selective CO_2 Photoreduction Enabled by Facet-Resolved Redox-Active Sites on Colloidal CdS Nanosheets. *J. Am. Chem. Soc.* **2022**, *144*, 16974–16983. [CrossRef]
50. Yang, Z.; Wang, S.; Zhang, Z.; Guo, W.; Jie, K.; Hashim, M.I.; Miljanić, O.Š.; Jiang, D.; Popovs, I.; Dai, S. Influence of Fluorination on CO_2 Adsorption in Materials Derived from Fluorinated Covalent Triazine Framework Precursors. *J. Mater. Chem. A* **2019**, *7*, 17277–17282. [CrossRef]
51. Sathish, C.; Premkumar, S.; Chu, X.; Yu, X.; Breese, M.B.H.; Al-Abri, M.; Al-Muhtaseb, A.H.; Karakoti, A.; Yi, J.; Vinu, A. Microporous Carbon Nitride ($C_3N_{5.4}$) with Tetrazine Based Molecular Structure for Efficient Adsorption of CO_2 and Water. *Angew. Chem. Int. Ed.* **2021**, *60*, 21242–21249. [CrossRef] [PubMed]
52. Liao, W.; Yang, Z.; Wang, Y.; Li, S.; Wang, C.; Zhou, Z. Novel Z-Scheme Nb_2O_5/C_3N_5 Photocatalyst for Boosted Degradation of Tetracycline Antibiotics by Visible Light-Assisted Activation of Persulfate System. *Chem. Eng. J.* **2023**, *478*, 147346. [CrossRef]
53. Wang, H.; Yu, L.; Peng, J.; Zou, J.; Gong, W.; Jiang, J. Experimental and Theoretical Investigation of Sulfur-Doped g-C_3N_4nanosheets/$FeCo_2O_4$ Nanorods S-Scheme Heterojunction for Photocatalytic H_2 Evolution. *Nano Res.* **2024**, *17*, 8007–8016. [CrossRef]

54. Xu, S.; Yu, Y.; Zhang, X.; Xue, D.; Wei, Y.; Xia, H.; Zhang, F.; Zhang, J. Enhanced Electron Delocalization Induced by Ferromagnetic Sulfur Doped C_3N_4 Triggers Selective H_2O_2 Production. *Angew. Chem. Int. Ed.* **2024**, *63*, e202407578.
55. Wang, X.; Maeda, K.; Thomas, A.; Takanabe, K.; Xin, G.; Carlsson, J.M.; Domen, K.; Antonietti, M. A Metal-Free Polymeric Photocatalyst for Hydrogen Production from Water under Visible Light. *Nat. Mater.* **2009**, *8*, 76–80. [CrossRef]
56. Wang, Y.; Shang, X.; Shen, J.; Zhang, Z.; Wang, D.; Lin, J.; Wu, J.C.S.; Fu, X.; Wang, X.; Li, C. Direct and Indirect Z-Scheme Heterostructure-Coupled Photosystem Enabling Cooperation of CO_2 Reduction and H_2O Oxidation. *Nat. Commun.* **2020**, *11*, 3043. [CrossRef]
57. Cheng, L.; Yin, H.; Cai, C.; Fan, J.; Xiang, Q. Single Ni Atoms Anchored on Porous Few-Layer g-C_3N_4 for Photocatalytic CO_2 Reduction: The Role of Edge Confinement. *Small* **2020**, *16*, 2002411. [CrossRef] [PubMed]
58. Yu, G.; Liu, L.; Zhao, C.; Guo, S.; Meng, H.; Zhu, Y.; Zhang, X.-M. Enhanced Internal Electric Field of CdS/NU-M Z-Scheme Heterojunction for Efficient Photocatalytic Hydrogen Evolution. *Chem. Eng. J.* **2024**, *494*, 153099. [CrossRef]
59. Li, X.; Bai, Y.; Shi, X.; Huang, J.; Zhang, K.; Wang, R.; Ye, L. Mesoporous g-C_3N_4/MXene (Ti_3C_2Tx) Heterojunction as a 2D Electronic Charge Transfer for Efficient Photocatalytic CO_2 Reduction. *Appl. Surf. Sci.* **2021**, *546*, 149111. [CrossRef]
60. Wang, M.; Shen, M.; Zhang, L.; Tian, J.; Jin, X.; Zhou, Y.; Shi, J. 2D-2D MnO_2/g-C_3N_4 Heterojunction Photocatalyst: In-Situ Synthesis and Enhanced CO_2 Reduction Activity. *Carbon* **2017**, *120*, 23–31. [CrossRef]
61. Bhosale, R.; Jain, S.; Vinod, C.P.; Kumar, S.; Ogale, S. Direct Z-Scheme g-C_3N_4/$FeWO_4$ Nanocomposite for Enhanced and Selective Photocatalytic CO_2 Reduction under Visible Light. *ACS Appl. Mater. Interfaces* **2019**, *11*, 6174–6183. [CrossRef]
62. Li, M.; Zhang, L.; Wu, M.; Du, Y.; Fan, X.; Wang, M.; Zhang, L.; Kong, Q.; Shi, J. Mesostructured CeO_2/g-C_3N_4 Nanocomposites: Remarkably Enhanced Photocatalytic Activity for CO_2 Reduction by Mutual Component Activations. *Nano Energy* **2016**, *19*, 145–155. [CrossRef]